An RSS-Based Classification of User Equipment Usage in Indoor Millimeter Wave Wireless Networks Using Machine Learning

LEI ZHANG[1], (Student Member, IEEE), **YANG HUA**[1],
SIMON L. COTTON[1], (Senior Member, IEEE), **SEONG KI YOO**[2], (Member, IEEE),
CLAUDIO R. C. M. DA SILVA[3], (Senior Member, IEEE),
AND WILLIAM G. SCANLON[4], (Fellow, IEEE)

[1]Institute of Electronics, Communications and Information Technology, Queen's University Belfast, Belfast BT3 9DT, U.K.
[2]School of Computing, Electronics and Mathematics, Coventry University, Coventry CV1 5FB, U.K.
[3]Next Generation and Standards, Intel Corporation, Santa Clara, CA 95054, USA
[4]Tyndall National Institute, Cork T12R5CP, Ireland

Corresponding author: Simon L. Cotton (simon.cotton@qub.ac.uk)

ABSTRACT The use of millimeter wave technologies offer a promising solution for dense small cell networks, despite having to contend with challenging propagation characteristics. In particular, user-induced effects can lead to significant channel variations depending on the user equipment (UE) usage mode which in turn, can impact the quality of service. Estimation of UE operating conditions is therefore critical for optimal radio resource management. We propose a new approach to user activity recognition which makes use of both supervised and unsupervised machine learning. In particular, using information extracted from the received signal strength (RSS), a common metric readily available from many receiver chipsets, we perform a classification of user state (*static* or *mobile* relative to an access point) and UE mode of operation (*voice call, using an app* or *in pocket*). To develop and then train our classification system, measured RSS data was obtained using a custom 60 GHz measurement system for a range of indoor office scenarios which considered various UE to ceiling mounted access point configurations. In our approach, differentiation between *static* and *mobile* states is performed in preprocessing using a k-means algorithm. Small-scale fading features are then estimated from the RSS data and, using different feature scaling mechanisms, various supervised learning approaches are applied to investigate the optimal classification accuracy for the considered use cases in this work. We compare the classification performance of various window sizes and types, and show that a sliding window length of 1s without overlap performs best for time series segmentation at 60 GHz for the activities considered in this study. Among the different supervised learning approaches, the Decision Tree (DT) classifier performs best for both the user *static* and *mobile* cases with an accuracy of 100% and 98.0%, respectively. For *static* cases, user orientation, i.e., line-of-sight (LOS), quasi-LOS, and non-LOS, can also be classified and here the DT classifier also performs best with an accuracy of 98.2%, 97.6% and 100% for the *voice call*, *using an app* or *in pocket* use cases. Additionally, a feature ranking algorithm, called *ReliefF*, is adopted to determine the small-scale fading features that have the most significant influences on the classification accuracy and three different feature sets, namely *Full*, *Reduced* and *Constrained* sets, are then proposed based on feature ranking results. This allows the proposed techniques to be deployed on wireless platforms with different levels of processing capability.

INDEX TERMS Human activity recognition, millimeter wave, received signal strength, supervised learning, unsupervised learning, user equipment, wireless networks.

I. INTRODUCTION

Millimeter wave (mmWave) technologies are set to play an important role in supporting the explosive demands for

mobile broadband services which will occur over the next decade [1]. To help meet these requirements, the IEEE 802.11 Task Group ay (802.11ay) was formed in 2015 to define physical and medium access control layer amendments which will enable Wi-Fi devices to achieve 100 Gb/s using the significant bandwidth available in the unlicensed mmWave

spectrum [2]. Capitalizing on the bandwidth available at 60 GHz and the short-range propagation characteristics, mmWave technologies will help to facilitate network densification [3]. However, these smaller network topologies, where the access points (APs), or equivalently eNodeBs (eNBs) in cellular systems, are typically positioned at lower elevation compared to conventional systems are particularly prone to user-induced effects such as human body blockage and shadowing. While understanding these effects is essential for ensuring the success of future small cell deployments [4] within indoor environments, the APs (or eNBs) are usually placed at a height that is close to the ceiling in [5]–[8].

User-induced channel effects vary significantly with activity and user equipment (UE) operating mode and tend to be more pronounced at mmWave frequencies [9], [10]. One way to guarantee the quality of service QoS) at the user side and further evolve traditional wireless networks towards smart networks is to utilize network radio resource management (RRM) optimization techniques based on identifying the UE use case (e.g., making a call, texting messages etc.) and the user activity (e.g., walking, standing, sitting, laying down etc.) or whether the UE is in a line-of-sight (LOS)/Non-LOS (NLOS) condition relevant to the access point (AP) [11]–[15]. Furthermore, user activity recognition also provides opportunities to optimize emerging applications, such as smart home automation, entertainment, healthcare, safety protection and well-being monitoring/management [16], [17].

One approach often employed in the literature makes use of wearable sensors. The application of wearable sensors can be broadly categorized into one of three groups namely: received signal strength (RSS)/RSS Indicator (RSSI) or Radio Frequency (RF) signal based; inertial sensor data based; and finally the combination of the RSS/RSSI and inertial sensor data based methods. Considering the RSS/RSSI-based method, Geng *et al.* [18] proposed a RF based motion classification approach combined with some statistical measures obtained from the RSS collected by on-body sensors. These metrics included mean, variance, level crossing rate (LCR) and fading duration, etc. A Support Vector Machine (SVM) [19] was utilized in the classifier and an accuracy of between 82.7% and 90.4% was obtained for correctly identifying human motions, e.g., standing, walking and running, etc. The authors of [20] classified a series of human motions, such as running, walking, sitting, sleeping, etc., using the RSS data obtained from numerical simulation and measurement campaigns at 403.5 MHz and 2.45 GHz. It was found that the Back Propagation and SVM classifiers provided the best classification accuracy of between 63.8% and 95.7%. Similarly, in [21], Chi *et al.* proposed human activity recognition using monitoring middleware. This middleware, named *Harmony*, utilized coarse-grained RSS measurements from the radios of IoT devices at 2.45 GHz and a state-transition based Markov model was then applied to understand the states and events including the daily, accident, fitness and steady categories with an accuracy between 74% and 90%.

Now turning attention to the inertial sensor data based method, in [22], an inertial sensor coupled with a supervised based approach to learning was proposed. Using data collected by the tri-axial accelerometer and gyroscope of a smartphone, a series of statistical features were extracted from the time domain information, including the mean, standard deviation, and interquartile range as well as weighted average, skewness and kurtosis in the frequency domain. The authors of [22] proposed an online framework using Naive Bayes (NB) [23] and K-Nearest Neighbors (KNN) [24]. Both static user activities, e.g., standing, sitting, and laying down and dynamic user activities, e.g., walking and climbing up and down stairs were classified with an accuracy of up to 90.1%. In [25], a Single Layer Feedforward Neural Network with same carefully chosen features as in [22] was utilized to assist a Long Short-Term Memory network. Three-dimensional linear acceleration, total acceleration and gyroscope data from a smartphone was used to classify static and dynamic activities achieving an accuracy as high as 97.7%. Studies on the combination of RSS/RSSI and inertial sensor data based methods have included [26], which used a combined RSS and inertial sensor approach along with the Echo State Network to classify the daily user activities at 2.4 GHz (within the frequency band defined by the IEEE 802.15.4 standard), such as bending, cycling, laying, and walking etc., with an overall accuracy of between 95.6% and 98.8%. In [27], the RSSI, Transmission Control Protocol TCP) throughputs, cellular based-station IDs for Long-Term Evolution (LTE), together with acceleration sensor data were analyzed as a means of recognizing different user transportation modes, e.g., static, walking, riding a bicycle, on a bus or a train, etc. A convolutional neural network (CNN) model was applied to the data, providing a classification accuracy of between 77.0% and 96.5%. While clearly proficient at estimating user activity, these sensor based approaches do require supplementary sensors, data analysis, and processing capability at the UE.

Another popular approach commonly used for activity recognition in wireless networking is vision-based, typically requiring video camera monitoring to recognize different human actions. For instance, mmWave human blockage prediction using RGB-D (depth) cameras was used to assisted with handovers in [28]. A test-bed consisting of a Kinect sensor [29] and IEEE 802.11 ad compliant WLAN devices was constructed to estimate the position and velocity of pedestrians, with the aim of avoiding throughput degradation by predicting potential human body blockage incidents. Moreover, Okamoto *et al.* studied throughput estimation at mmWave frequencies using images from an RGB-D camera along with machine learning [30]. An online algorithm, called adaptive regularization of weight vectors, was applied to process the image depth, thus building a relationship between image depth and unexpected throughput degradation. Although human blockage at mmWave frequencies has been effectively avoided in these studies, the application of video cameras is not always practical, for example when

the necessary infrastructure is unavailable or where there are privacy concerns. Furthermore, image processing can be computationally expensive, which may mean that it may not be able to adapt in response to the the real-time nature of wireless communications.

Motivated by the need for accurate user activity recognition in mmWave networks and some of the limitations of the previously discussed work, we propose a combined supervised and unsupervised approach that is able to recognize UE use case and user activity for indoor scenarios. An extensive mmWave measurement campaign involving different user states and some common UE use cases has been conducted in an indoor office measurement environment considering a ceiling-mounted wireless AP. Subsequently, a series of small-scale fading features of the mmWave channel are correctly extracted after an unsupervised preprocessing stage and various supervised classifiers are trained based on the extracted small-scale fading features. We compare the classification accuracy and computation performance of different supervised classifiers, namely multi-SVM, Decision Tree (DT) [31], NB, and Ensemble Learning (EL) [32]. Moreover, we investigate the influence of various RSS segmentation window types and sizes on the classification accuracy. Furthermore, by using a feature ranking algorithm, called *ReliefF* [33], we determine the most significant small-scale fading features which should be used to train the supervised classifier at 60 GHz for UE usage identification. Based on the feature ranking results, we demonstrate feature subsets with reduced dimensions which will be suitable for implementation on platforms with differing processing ability.

The remainder of this paper is organized as follows. The proposed automated classification approach is presented in Section II. The custom 60 GHz measurement system and measurement scenarios are described in Section III. A description of the measurement data and how it is processed is given in Section IV. Section V firstly investigates the effects of choosing the correct window size and type to provide the optimal classification performance at 60 GHz. Afterwards, the results of applying the classification techniques to the empirical mmWave channel data collected during our experiments are discussed and some insights related to different subsets of the selected features is also presented. Finally, the conclusions are summarized in Section VI.

II. CLASSIFICATION METHODOLOGY

The proposed classification system is illustrated in Fig. 1. There are five key stages which make up the system. These are (1) data preprocessing, (2) data segmentation and labeling, (3) RSS feature extraction, (4) RSS feature scaling, and (5) supervised learning based classification. After preprocessing, the system segments the user state into either *static* or *mobile* scenarios. The UE use cases for both *static* and *mobile* can be classified after the supervised learning based classification. In particular, for the user *static* scenario,
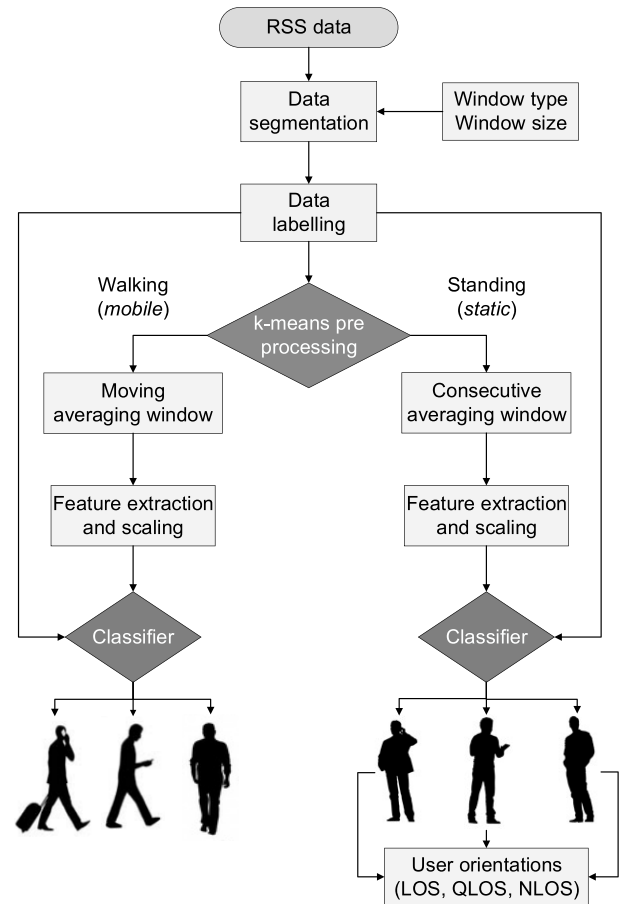

FIGURE 1. Flow diagram indicating the different stages of the proposed classification system.

user orientation (LOS, QLOS, and NLOS) is additionally classified.

Fig. 2 illustrates the geometry of the different measurement scenarios. As can be seen, three common UE use cases are considered in this study: (1) *Call* scenario, where the user holds the UE at his right ear while imitating the action of making a voice call; (2) *App* scenario, where the user holds the UE with his two hands in front of his chest, replicating the behavior of using an application; (3) *Pocket* scenario, where the user keeps the UE in the right waist pocket of his clothing. Consequently, the antenna boresight was oriented outwards away from the user's right ear, front chest, and right waist pocket for the *Call*, *App* and *Pocket* scenarios, respectively. In addition, in the *static* scenario, the LOS, QLOS and NLOS cases are specified in terms of the orientation angle relative to the direct geometric path to the wireless AP, i.e. 0° for LOS, 90°/270° for QLOS and 180° for NLOS cases, respectively. The relationship between the orientation angles (0°, 90°/270° and 180°) relative to the wireless AP and the user orientations (LOS, QLOS and NLOS) was investigated in [34], [35]. We have followed this convention for the UE orientations in the measurement set-up within this work.
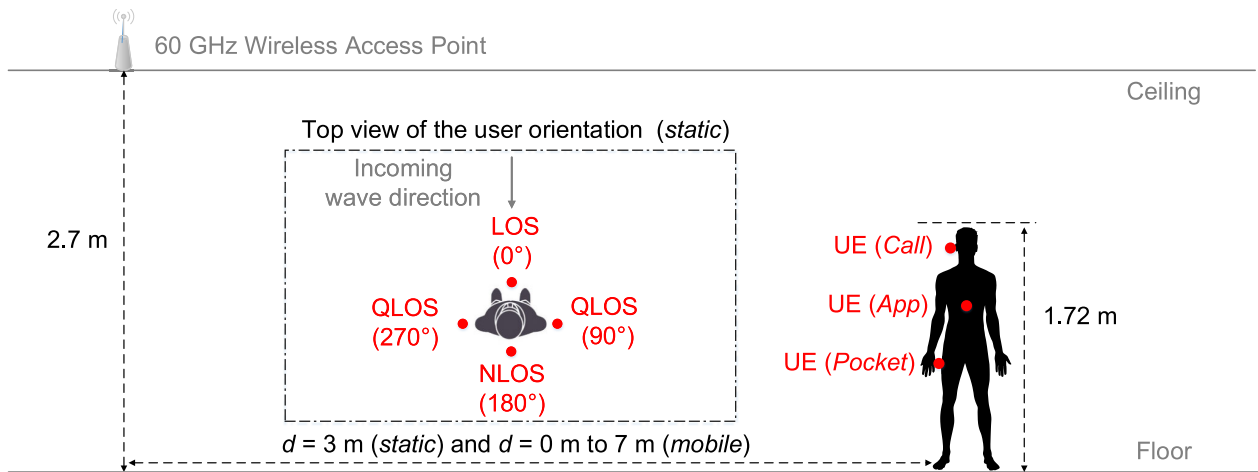
FIGURE 2. Geometry of measurement scenarios.

A. DATA SEGMENTATION AND LABELING

Windowing approaches are normally used for time-series signal segmentation in human activity recognition [36]. In this work, sliding windows with overlap and without overlap have both been applied in the data segmentation stage to investigate the optimal window type for 60 GHz indoor scenarios. Given that T is the sliding window size and the overlap ratio is defined as p ($0 \leq p < 1$), thus the overlap size is given by $T * p$. Suppose there are N available RSS segments in total after the data segmentation process, the RSS vector $\boldsymbol{R}$ can be defined as

$$\boldsymbol{R} = [\boldsymbol{R}_1, \ldots, \boldsymbol{R}_n, \ldots, \boldsymbol{R}_N], \quad (1 \leq n \leq N) \quad (1)$$

where $\boldsymbol{R}_n$ is the RSS vector of the n-th segment, thus $\boldsymbol{R}_n$ can be written as follows

$$\boldsymbol{R}_n = \left[r_n^1, \ldots, r_n^t, \ldots, r_n^T \right], \quad (1 \leq t \leq T) \quad (2)$$

where r_n^t is the linear RSS value at time instant t in the n-th segment. Afterwards, the labels are assigned in the data labeling stage for later used by the supervised learning based classifier. The label vector $\boldsymbol{L}$ is denoted as

$$\boldsymbol{L} = [L_1, \ldots, L_n, \ldots, L_N], \quad (1 \leq n \leq N) \quad (3)$$

where L_n is the assigned label for the n-th RSS segment. It is relatively easy to assign the label, if only one activity occurs during one segmentation window, however, if more than one activity occurs within a segment, it becomes difficult to allocate the corresponding label. In this work, since we are more concerned about the current UE use case rather than the previous state, the label is assigned based on the latter state of the window segmentation, e.g., if the *Call* and *App* states occur in succession within the n-th segment, then the label L_n will be given as *App*.

B. K-MEANS PREPROCESSING

To extract the small-scale fading for analysis, the path loss and large-scale fading must first be removed. Typically,

the path loss and large-scale fading components can be acquired by applying a low-pass filter to the raw RSS data in the linear scale. However, the correct length of the low-pass filter depends on the actual user activities. For instance, in the *static* case, the path loss and large-scale fading can be assumed to be fairly constant, thus the length of low-pass filter can be conveniently set as exactly the same as the segmentation window size, However for the *mobile* case, the path loss and large-scale fading components can vary over time, thus following convention, we choose a length of ten wavelengths for the low pass filter [37]. At 60 GHz, this equates to a distance of 50 mm. The effective sampling rate of the RSS measurement system used in this study was 1 kHz, with a user walking speed of 1 m/s, the moving window size is exactly 50 samples. Due to choices of different lengths of low-pass filter window size, an initial decision on whether the user is standing static or walking needs to be made. For this purpose, unsupervised k-means clustering [38] is used. More precisely, the variance of the small-scale fading (on a logarithmic scale) in each segment and the cluster number of 2 are set as the inputs to the k-means algorithm.

An example of the output of the k-means preprocessing is shown in the top part of Fig. 3 which uses a segmentation window with no overlap (i.e., $T = 1000$ and $p = 0$) applied to the raw RSS. From the output, it can be seen that accurate state estimation can be achieved with approximately 99.8% success, verifying that the *static* and *mobile* activities can be accurately differentiated using this simple preprocessing technique. A detailed discussion on selecting the segmentation window type and size will be presented in Section V-A. Although a very high estimation accuracy was achieved at the preprocessing stage, incorrect estimation was still observed to occur. An example of this is illustrated in the bottom part of Fig. 3. The incorrect estimation occurs in the 84th segmentation element, as the segment element in fact consists of both *mobile* and *static* states. The majority of this element is dominated by the *mobile* state, however, as discussed in
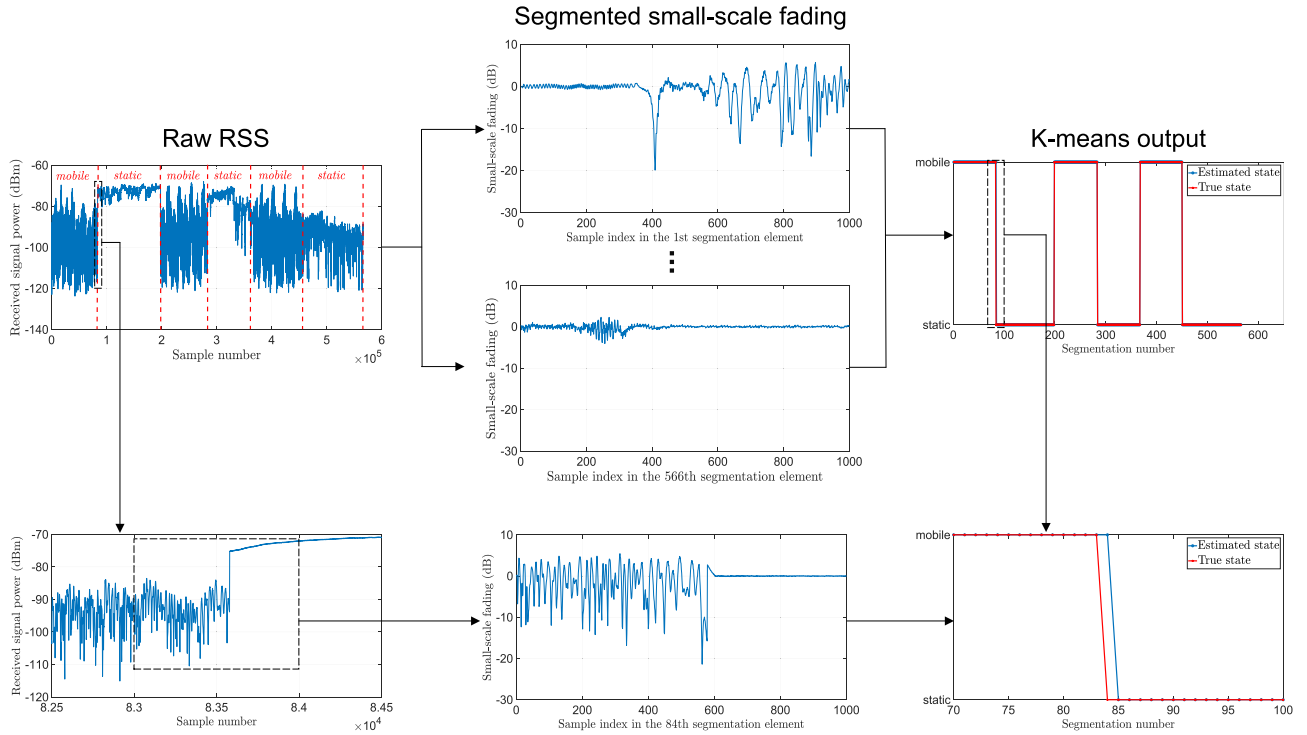
FIGURE 3. The output of k-means preprocessing with a segmentation window of size $T = 1000$ and no overlap $p = 0$ is shown at the top. Meanwhile, an example of where the k-mean preprocessing failed to estimate the correct state is demonstrated at the bottom.

Section II-A, the label allocated to this element is based on the more recent state, thus this type of incorrect estimation is unavoidable.

After the *static* and *mobile* activities are differentiated, the low-pass filter of correct window type and length will be applied on each RSS segment based on the estimated user activity. Thus the exact small-scale fading of the mmWave channel can be extracted and the small-scale fading vector $\boldsymbol{S}_n$ is obtained as

$$\boldsymbol{S}_n = [\boldsymbol{s}_1, \ldots, \boldsymbol{s}_n, \ldots, \boldsymbol{s}_N], \quad (1 \le n \le N) \qquad (4)$$

where $\boldsymbol{s}_n$ is the linear small-scale fading of the n-th segment and $\boldsymbol{s}_n$ can be expressed as

$$\boldsymbol{s}_n = \left[s_n^1, \ldots, s_n^t, \ldots, s_n^T \right], \quad (1 \le t \le T) \qquad (5)$$

where s_n^t is the linear small-scale fading of time instant t in the n-th segment. Correspondingly, the small-scale fading of the n-th segment in the logarithmic scale, denoted as $\boldsymbol{y}_n$, can be calculated as

$$\boldsymbol{y}_n = 20 \cdot \log_{10}(\boldsymbol{s}_n). \qquad (6)$$

C. SMALL-SCALE FADING FEATURE EXTRACTION

Six statistical features were extracted from the segmented small-scale fading time-series in this work: 1) variance, 2) Rice $\mathcal{K}$ factor, 3) Nakagami m parameter, 4) channel coherence time, 5) AFD, and 6) LCR. Details of each feature in the n-th segment are shown as follows

1) VARIANCE

$$\mathrm{Var}\left[\boldsymbol{y}_n\right] = \frac{1}{T-1} \sum_{t=1}^{T} \left| y_n^t - \frac{1}{T} \sum_{q=1}^{T} y_n^q \right|^2 \qquad (7)$$

where y_n^t is the logarithmic small-scale fading at the time instant t in the n-th segment.

2) RICE $\mathcal{K}$ FACTOR

The probability density function (PDF) of Rice distribution [39] is defined by

$$p(\boldsymbol{s}_n | \hat{v}, \hat{\sigma}) = \frac{\boldsymbol{s}_n}{\hat{\sigma}^2} \exp\left\{ \frac{-\left[(\boldsymbol{s}_n)^2 + \hat{v}^2 \right]}{2\hat{\sigma}^2} \right\} I_0\left(\frac{\boldsymbol{s}_n \hat{v}}{\hat{\sigma}^2} \right) \qquad (8)$$

where $\hat{v}$ and $\hat{\sigma}$ are estimated Rice shape parameters. The Rice $\mathcal{K}$ factor, which characterizes the ratio between the power carried by the LOS component and the power contained the scattered waves, is defined as

$$\mathcal{K}(\boldsymbol{s}_n) = \frac{\hat{v}^2}{2\hat{\sigma}^2}. \qquad (9)$$

3) NAKAGAMI m PARAMETER

The PDF of the Nakagami distribution [40] may be written as

$$p(\boldsymbol{s}_n; \hat{m}, \hat{\Omega}) = \frac{2\hat{m}^{\hat{m}}}{\Gamma(\hat{m})\hat{\Omega}^{\hat{m}}} (\boldsymbol{s}_n)^{2\hat{m}-1} \exp\left[-\frac{\hat{m}}{\hat{\Omega}} (\boldsymbol{s}_n)^2 \right] \qquad (10)$$

where $\hat{\Omega}$ ($\hat{\Omega} > 0$) is the estimated parameter controls the spread and $\hat{m}$ ($\hat{m} > 0.5$) is the estimated shape parameter,

which represents the multipath fading severity and defined by

$$\hat{m}(s_n) = \frac{\mathbb{E}^2\left[(s_n)^2\right]}{\text{Var}\left[(s_n)^2\right]}. \tag{11}$$

4) CHANNEL COHERENCE TIME

The time-series autocorrelation function (ACF) for time lag i [41] is given by

$$R_i = \frac{c_i}{c_0} = \frac{c_i}{\text{Var}[s_n]} \tag{12}$$

where c_i is the autocovariance function of time lag i and defined as

$$c_i = \frac{1}{T}\sum_{t=1}^{T-i}\left(s_n^t - \frac{1}{T}\sum_{q=1}^{T}s_n^q\right)\left(s_n^{t+i} - \frac{1}{T}\sum_{q=1}^{T}s_n^q\right) \tag{13}$$

and the channel coherence time $\mathcal{T}_c$ is defined as

$$\mathcal{T}_c(\gamma) = i(R_i > \gamma) \cdot \mathcal{T}_s \tag{14}$$

where γ ($0 < \gamma < 1$) is a selected ACF threshold and $\mathcal{T}_s$ represents the sampling time.

5) AFD

The AFD is defined as the average time duration of a fading event [42]. The empirical AFD below a pre-defined threshold δ may be written as

$$\text{AFD}(y_n, \delta) = \frac{d\left(y_n^t < \delta\right)}{\mathcal{N}(y_n^t < \delta)} \tag{15}$$

where d denotes the overall time duration of fading events below a threshold δ within the n-th segment, and $\mathcal{N}$ denotes the total number of fading events within the n-th segment.

6) LCR

The LCR is defined by the average number of times per second that a fading signal crosses a pre-defined threshold δ [42]. It is given by

$$\text{LCR}(y_n, \delta) = \frac{\mathcal{N}(y_n^t < \delta)}{T}. \tag{16}$$

The rationale for choosing the Rice $\mathcal{K}$ factor and Nakagami m parameter features is that both models have shown a good fit to the small-scale fading observed in 60 GHz small cell deployments [9]. Additionally, as shown in [43], the second-order statistics, such as AFD and LCR, are highly correlated to different UE use cases. Therefore, the UE use cases could potentially be classified by exploiting the characteristics of these statistical features. The Rice $\mathcal{K}$ factor and Nakagami m parameter were estimated using maximum likelihood estimation (MLE) performed in MATLAB, the first empirical ACF threshold γ was selected to be 0.5, since the coherence time is defined as the time over which the ACF is above 0.5 [44]. A second ACF threshold γ of 0, indicating the first time instance that the small-scale fading observed to become entirely decorrelated, was also selected. It can be

seen from Fig. 3 that the majority of the small-scale fading occurred in the range of -20 dB to 10 dB. Subsequently, δ was set between $[-20, 10]$ dB with a 1 dB step size. As a result, the dimensions of the adopted statistical features were $N \times 67$ in the proposed approach.

D. SMALL-SCALE FADING FEATURE SCALING

During the exploratory data analysis, it was noticed that the range of each feature's values varies widely. If one feature's value has a much broader range than the others, it is very likely that the object function's distance of the classifier could be dominated by this wide-range feature [45]. Additionally, it is known that the gradient descent converges much faster with feature scaling than without it [46]. For these reasons, the values of all features were scaled before being used as an input to a classifier. This scaling process is also known as feature normalization. There are four different scaling mechanisms adopted in this work, namely: 1) min-max normalization (*min-max*) [47], 2) mean normalization (*mean*) [48], 3) standardization (*standard*) [49], and 4) unit length scaling (*unit length*) [50]. Each of the scaling mechanisms is defined below where f_j denotes the j-th extracted feature before normalization, while f_j' denotes the j-th normalized feature:

1) MIN-MAX

$$f_j' = \frac{f_j - \min(f_j)}{\max(f_j) - \min(f_j)} \tag{17}$$

where $\max(f_j)$ and $\min(f_j)$ denote the maximum and minimum value of the j-th extracted feature, respectively.

2) MEAN

$$f_j' = \frac{f_j - \bar{f}_j}{\max(f_j) - \min(f_j)} \tag{18}$$

where $\bar{f}_j$ denotes the mean value of the the j-th extracted feature.

3) STANDARD

$$f_j' = \frac{f_j - \bar{f}_j}{\text{Std}(f_j)} \tag{19}$$

where $\text{Std}(f_j)$ denotes the standard deviation of the j-th extracted feature.

4) UNIT LENGTH

$$f_j' = \frac{f_j}{\|f_j\|} \tag{20}$$

where $\|f_j\|$ denotes the l^2-norm of the j-th extracted feature.

E. SUPERVISED LEARNING BASED CLASSIFIER

As shown in Fig. 1, the input provided to the supervised learning based classifier are the scaled RSS statistical features and the assigned data labels. It is noted that the order of the
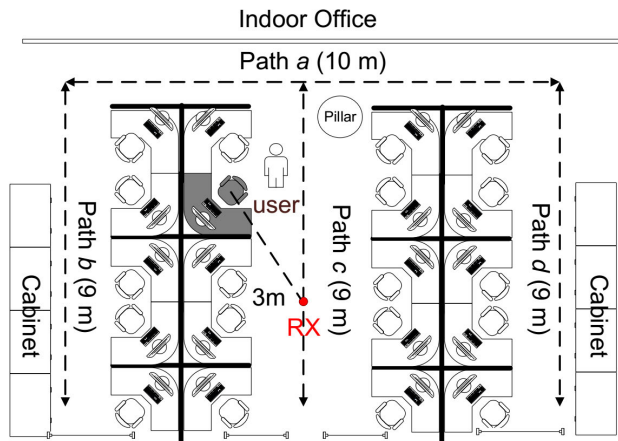
Indoor Office

Path *a* (10 m)

FIGURE 4. Floor plan for mmWave indoor measurement scenario.

input features is as described in Section II-C, i.e., starting from the Var through to LCR. Furthermore, aiming to train the corresponding classifier model, the data is partitioned randomly into three parts, i.e., training, validation and test data. Additionally, 10-fold cross validation [51] has been performed to ensure that the trained classifier model is independent of the unknown data set and avoids the problem of overfitting or selection bias. In 10-fold cross validation, the segmented data is randomly partitioned into 10 equal-size sub-samples. Subsequently, a single sub-sample is retrained as validating data, while the remaining 9 sub-samples are used as training data. In this way, the cross-validation is repeated 10 times and these results are averaged to produce a unique estimation.

III. EXPERIMENTAL SET-UP

The custom 60 GHz wireless channel measurement system used in this study was based on the HMC6000LP711E transmitter (TX) and HMC6001LP711E receiver (RX) modules manufactured by Analog Devices. Both units featured an identical linearly-polarized antenna-in-package with +7.5 dBi gain. The measured half power beam width (HPBW) of the antenna is approximately 120° [52]. At the beginning of each set of measurements, the TX was configured to transmit a continuous wave signal at 60.05 GHz with an Equivalent Isotropically Radiated Power (EIRP) of +10.9 dBm. The received signal power at the RX was recorded using a v1.4 Red Pitaya data acquisition platform at a sample rate of 96 kHz. Afterwards, the data was downsampled by averaging 96 consecutive samples to improve the signal to noise ratio (SNR) performance, thus giving an effective sampling rate of 1 kHz after downsampling.

The measurements were conducted in an open office area (10.62 m × 12.23 m) [53], located on the first floor of the ECIT Institute, Queen's University Belfast, UK, as illustrated in Fig. 4. The indoor office area consists of metal studded dry wall with a metal tiled floor covered with polypropylene fiber, rubber backed carpet tiles and metal ceiling with mineral fiber tiles and recessed louvered luminaries suspended

2.70 m above the floor level. It also contained a number of soft partitions, cabinets, PCs, chairs and desks. During the measurements, the RX board was placed above the ceiling at the point indicated by the red circle (Fig. 4), with the antenna boresight facing downwards, i.e., towards the floor, emulating a mmWave wireless AP. The TX board was fixed to the inside of a compact acrylonitrile butadiene styrene (ABS) enclosure, allowing the test user to carry the TX board as they would a smart phone during the measurement process. The test user was an adult male of height of 1.72 m and mass 75 kg. Additionally, the horizontal, i.e., floor projected distance between the mmWave AP and the test user was always maintained at 3 m for the *static* scenarios and varied from 0 m to 7 m for the *mobile* scenarios, respectively.

During the *mobile* scenarios, the user walked at a constant speed of approximately 1 m/s along different paths (in both directions), i.e., Path *a*, *b*, *c*, and *d* as shown in Fig. 4. The lengths of Path *a*, *b*, *c*, and *d* are 10 m, 9 m, 9 m and 9 m, respectively. The user alternated between each of UE use cases (*Call*, *App* and *Pocket*) in a random manner. For the *static* scenario, measurements were conducted in the gray color-filled area indicated in Fig. 4 during which the user stood stationary and randomly cycled through the UE use cases. A digital camera was utilized to record the experiments and generate the ground truth of the measurement as well as the labels for the training data.

IV. DATA VALIDATION

To improve the robustness of the measurement results, each of the aforementioned measurement scenarios were repeated three times. Afterwards, all of the collected RSS data was fed in to the data segmentation stage of the classification system, as shown in Fig. 1. The overall measurement data set consisted of approximately 570,000 samples, equivalently 570s length in time (210s for the *mobile* scenarios and 360s for the *static* scenarios). This included the measurement data for all the four mobile paths, i.e., paths *a*, *b*, *c*, and *d*, to make sure that the small-scale fading for various user walking cases was fully captured. In the *static* scenarios, the minimum duration for each user orientation (LOS, QLOS and NLOS) measurement was 10s to ensure that various physiological effects such as breathing were adequately recorded. Subsequently, the data was randomly divided into three independent sets, i.e., training (70%), validation (15%) and test sets (15%). Additionally, the 10-fold cross validation (described in Section II-E) was performed on the acquired data to make sure that the problem of overfitting can be effectively avoided.

V. RESULTS AND ANALYSIS
A. EFFECTS OF VARIOUS WINDOW SIZES AND TYPES
After obtaining the measurement data from the *mobile* state (including different walking paths) and *static* state (including various user orientations), firstly the RSS data needs to be segmented as described in Section II-A. Nonetheless, choosing the optimal window type and size for the RSS segmentation is a critical issue in the classification process.
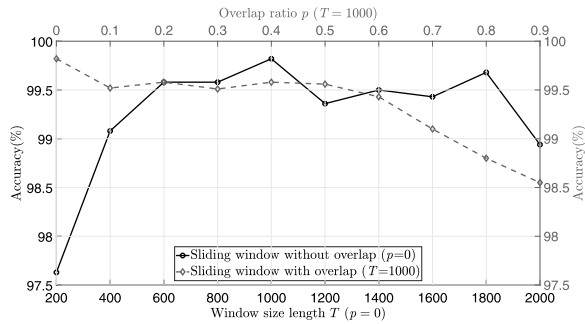
FIGURE 5. Effect of various window sizes and types upon classification accuracy.

On one hand, a larger window size is needed for complex activities but requires more computational resources. On the other hand, a smaller window size enables a faster recognition rate, but the limited information in the smaller window may result in poorer classification performance. Generally speaking, there is not a specific optimal window type and size for activity recognition work, the selected window type and size is often dependent on the device and system requirements [36].

The classification accuracy performance after k-means preprocessing for different window types is presented in Fig. 5. Specifically, the performance of various sliding window sizes T without overlap ($p = 0$) and sliding windows with different overlapping ratios for the $T = 1000$ case are shown. As the RSS sampling rate in this work was 1 kHz, the time duration of each segmentation window of $T = 1000$ is exactly $T/1000 = 1$s. The highest classification accuracy obtained was 99.8% for $T = 1000$ and $p = 0$. Thus this segmentation format was used to obtain the results presented in the remainder of this paper. Additionally, the *mean* normalization described in Section II-D was observed to provide the highest classification accuracy throughout all the considered scenarios, thus it is also adopted in the sequel.

B. PERFORMANCE METRICS

A *confusion matrix*, also know as an *error matrix*, allows the visualization of an algorithm's performance in statistical classification problems. In a typical *confusion matrix*, each row of the matrix represents the instances in a predicted/output class, while each column represents the instances in an actual/target class. The diagonal cells correspond to ratios of observations that are correctly classified and the off-diagonal cells correspond to ratios of incorrectly classified observations. Additionally, the *Recall*, also called *true positive rate (TPR)* and *Precision*, also called *positive predictive value (PPV)* metrics are also provided in the confusion matrices given in Tables 1 to 7. *Recall* is defined by the fraction of the number of correct positive results and the number of positive results that should have been returned, while *Precision* is defined by the fraction of the number of correct positive results and the number of all positive results predicted in the

TABLE 1. Confusion matrix for multi-class SVM classifier.

(a) Confusion matrix for SVM classifier – *mobile* scenarios

Accuracy	Call	App	Pocket	*Precision*
Call	1.0	0.0	0.0	1.0
App	0.125	0.875	0.0	0.875
Pocket	0.0	0.0	1.0	1.0
Recall	0.875	1.0	1.0	0.947
MCC			0.94	

(b) Confusion matrix for SVM classifier – *static* scenarios

Accuracy	Call	App	Pocket	*Precision*
Call	0.882	0.059	0.059	0.882
App	0.0	0.857	0.143	0.857
Pocket	0.0	0.083	0.917	0.917
Recall	1.0	0.706	0.824	0.837
MCC			0.8299	

test set. The values of *Recall* and *Precision* are given by

$$\text{Recall} = \frac{TP}{P} = \frac{TP}{TP + FN} \qquad (21)$$

$$\text{Precision} = \frac{TP}{\hat{P}} = \frac{TP}{TP + FP} \qquad (22)$$

where TP is the number of true positive samples, P is the number of all actual positive results, FN is the number of false negative samples, $\hat{P}$ is the number of all predicted positive results and FP is the number of false positive samples. Also, the overall accuracy of correctly classified classes is given in the bottom right corner (boxed) of the confusion matrix table, i.e., the cross-section of the *Recall* and *Precision* entries

Moreover, in order to consider both the *Precision* and *Recall* of the test to compute the score of classification accuracy, the *F-measure* [54] and *Matthews correlation coefficient (MCC)* [55] are commonly applied in the machine learning field. The main difference between the *F-measure* and *MCC* is that, MCC takes into account TP, true negative (TN), FP, and FN even if the classes are of very different sizes, while the *F-measure* does not include TN and performs better when the sizes of classes are exactly same. In this work, since the time the user spends in each UE use case may be slightly different, we adopt MCC as the classification score for our proposed recognition approach. The MCC under the multi-class case, also called the R_U statistic (for U classes), is generally defined in terms of a $U \times U$-size confusion matrix V in [56] and shown in Equation (23), as shown at the bottom of the netx page. In Equation (23), V_{uv} corresponds to the element of u-th row and v-th column in the confusion matrix V and $\{u, u', v, v', z \in \mathbb{Z} : 1 \leq u, u', v, v', z \leq U\} = \{1, 2, \ldots, U\}$. The maximum value of MCC is always $+1$ and the minimum value will be between -1 and 0 depending on the true

TABLE 2. Confusion matrix for Decision Tree classifier.

(a) Confusion matrix for DT classifier – *mobile* scenarios				
Accuracy	Call	App	Pocket	*Precision*
Call	1.0	0.0	0.0	1.0
App	0.0	1.0	0.0	1.0
Pocket	0.0	0.0	1.0	1.0
Recall	1.0	1.0	1.0	1.0
MCC				1.0
(b) Confusion matrix for DT classifier – *static* scenarios				
Accuracy	Call	App	Pocket	*Precision*
Call	1.0	0.0	0.0	1.0
App	0.0	1.0	0.0	1.0
Pocket	0.0	0.056	0.944	0.944
Recall	1.0	0.941	1.0	0.980
MCC				0.9725

TABLE 4. Confusion matrix for EL classifier.

(a) Confusion matrix for EL classifier – *mobile* scenarios				
Accuracy	Call	App	Pocket	*Precision*
Call	1.0	0.0	0.0	1.0
App	0.143	0.857	0.0	0.857
Pocket	0.0	0.2	0.8	0.8
Recall	0.875	0.857	1.0	0.895
MCC				0.8329
(b) Confusion matrix for EL classifier – *static* scenarios				
Accuracy	Call	App	Pocket	*Precision*
Call	0.838	0.063	0.1	0.938
App	0.0	0.789	0.211	0.789
Pocket	0.0	0.071	0.929	0.929
Recall	1.0	0.882	0.765	0.878
MCC				0.7835

TABLE 3. Confusion matrix for Naive Bayes classifier.

(a) Confusion matrix for NB classifier – *mobile* scenarios				
Accuracy	Call	App	Pocket	*Precision*
Call	1.0	0.0	0.0	1.0
App	0.278	0.444	0.278	0.444
Pocket	0.0	0.111	0.889	0.889
Recall	0.688	0.889	0.615	0.711
MCC				0.684
(b) Confusion matrix for NB classifier – *static* scenarios				
Accuracy	Call	App	Pocket	*Precision*
Call	0.424	0.273	0.303	0.424
App	0.111	0.889	0.0	0.889
Pocket	0.0	0.0	1.0	1.0
Recall	0.933	0.471	0.412	0.592
MCC				0.6756

C. UE USE CLASSIFICATION RESULTS

Following the approach described above and illustrated in Fig. 1, classification results for different UE use cases using each classifier were obtained and are given in Tables 1 to 4. As we can see, the DT classifier outperforms all others with an accuracy of 100% (MCC: 1.0) and 98.0% (MCC: 0.9725) for both *mobile* and *static* activities, respectively. The NB classifier performs worst in both *mobile* and *static* cases, with an accuracy of 71.1% (MCC: 0.684) and 59.2% (MCC: 0.6756). The reason for this is that the statistical features we adopted in this work are potentially highly correlated, whereas the assumption of the NB classifier is that the features are non-correlated. Furthermore, for every classifier the accuracy performance for the *mobile* activity is better than *static* activity. For example, with the EL classifier (Table 4), the overall accuracy is 89.5% (MCC: 0.8329) in the *mobile* scenario, compared to 87.8% (MCC: 0.7835) for the *static* scenario. The main reason for this is that in the *mobile* scenario, the statistics of small-scale fading are highly correlated with the UE use cases [43], i.e., how the UE is handled by the user. However, in the *static* scenario, in addition to how the user is handing the UE, user breathing and vibration effects cannot be neglected at mmWave frequencies. Hence the statistics of small-scale fading are more likely to be quasi-stationary or non-stationary [57].

distribution. Consequently, an MCC of +1 represents a perfect prediction, 0 means no better than random prediction and negative MCC values indicate a great disagreement between prediction and observation.

$$MCC = \frac{\sum_u \sum_v \sum_z (V_{uu}V_{vz} - V_{uv}V_{zu})}{\sqrt{\sum_u (\sum_v V_{uv})(\sum_{u'|u' \neq u} \sum_{v'} V_{u'v'})} \sqrt{\sum_u (\sum_v V_{vu})(\sum_{u'|u' \neq u} \sum_{v'} V_{v'u'})}} \tag{23}$$

TABLE 5. User orientation confusion matrix for the *Call* case.

(a) Confusion matrix for multi-class SVM classifier

Accuracy	LOS	QLOS	NLOS	*Precision*
LOS	0.958	0.042	0.0	0.958
QLOS	0.0	1.0	0.0	1.0
NLOS	0.0	0.0	1.0	1.0
Recall	1.0	0.938	1.0	0.982
MCC		0.9793		

(b) Confusion matrix for DT classifier

Accuracy	LOS	QLOS	NLOS	*Precision*
LOS	1.0	0.0	0.0	1.0
QLOS	0.0	1.0	0.0	1.0
NLOS	0.0	0.056	0.944	0.944
Recall	1.0	0.938	1.0	0.982
MCC		0.9725		

(c) Confusion matrix for NB classifier

Accuracy	LOS	QLOS	NLOS	*Precision*
LOS	0.84	0.08	0.08	0.84
QLOS	0.2	0.8	0.0	0.8
NLOS	0.0	0.286	0.714	0.714
Recall	0.913	0.50	0.882	0.786
MCC		0.6811		

(d) Confusion matrix for EL classifier

Accuracy	LOS	QLOS	NLOS	*Precision*
LOS	1.0	0.0	0.0	1.0
QLOS	0.0	1.0	0.0	1.0
NLOS	0.0	0.0	1.0	1.0
Recall	1.0	1.0	1.0	1.0
MCC		1.0		

TABLE 6. User orientation confusion matrix for the *App* case.

(a) Confusion matrix for multi-class SVM classifier

Accuracy	LOS	QLOS	NLOS	*Precision*
LOS	0.917	0.083	0.0	0.917
QLOS	0.0	0.923	0.077	0.923
NLOS	0.0	0.063	0.938	0.938
Recall	1.0	0.857	0.938	0.927
MCC		0.8894		

(b) Confusion matrix for DT classifier

Accuracy	LOS	QLOS	NLOS	*Precision*
LOS	1.0	0.0	0.0	1.0
QLOS	0.067	0.933	0.0	0.933
NLOS	0.0	0.0	1.0	1.0
Recall	0.909	1.0	1.0	0.976
MCC		0.9672		

(c) Confusion matrix for NB classifier

Accuracy	LOS	QLOS	NLOS	*Precision*
LOS	1.0	0.0	0.0	1.0
QLOS	0.2	0.5	0.3	0.5
NLOS	0.067	0.267	0.667	0.667
Recall	0.545	0.714	0.625	0.634
MCC		0.5894		

(d) Confusion matrix for EL classifier

Accuracy	LOS	QLOS	NLOS	*Precision*
LOS	0.727	0.182	0.091	0.727
QLOS	0.0	0.625	0.375	0.625
NLOS	0.214	0.143	0.643	0.643
Recall	0.727	0.714	0.563	0.659
MCC		0.4982		

D. USER ORIENTATION CLASSIFICATION RESULTS

The user orientation estimation results are provided in Tables 5 to 7. Again, the DT classifier performs better and is more robust than the other classifiers with an accuracy of 98.2% (MCC: 0.9725), 97.6% (MCC: 0.9672) and 100% (MCC: 1) for the *Call*, *App*, and *Pocket* cases, respectively. Furthermore, the classification accuracy for the *Call* case is higher than the *App* and *Pocket* scenarios. For example, for the multi-class SVM classifier, the overall classification accuracy for the *Call* case is 98.2% (MCC: 0.9793) and only 92.7% (MCC: 0.8894) and 85.4% (MCC: 0.7807) for *App* and *Pocket*, respectively. A possible explanation for this is due to the fact that in the *Call* scenario, the user was holding the UE very close to the ear position at a higher elevation, with the antenna boresight facing away from the body, thus more strongly differentiating between the LOS, QLOS and NLOS cases than those in the *App* and *Pocket* scenarios. It is also interesting that the *App* and *Pocket* scenarios are difficult to recognize under QLOS conditions. For example, in the confusion matrix of the EL classifier in Table 6 and Table 7, the precision of QLOS is 62.5% (*App*) and 88.9% (*Pocket*), while the precision of LOS is 72.7% (*App*) and 93.8% (*Pocket*) and the precision of NLOS is 64.3% (*App*) and 93.8% (*Pocket*), respectively. This indicates for the *App* and *Pocket* scenarios, the differences between QLOS and LOS/NLOS are not always clear as the antenna boresight is facing towards the floor in the *App* case and the UE is positioned at a lower elevation in the pocket in the *Pocket* case.

TABLE 7. User orientation confusion matrix for the *Pocket* case.

(a) Confusion matrix for multi-class SVM classifier

Accuracy	LOS	QLOS	NLOS	*Precision*
LOS	0.857	0.071	0.071	0.857
QLOS	0.308	0.692	0.0	0.692
NLOS	0.0	0.0	1.0	1.0
Recall	0.75	0.90	0.933	0.854
MCC		0.7807		

(b) Confusion matrix for DT classifier

Accuracy	LOS	QLOS	NLOS	*Precision*
LOS	1.0	0.0	0.0	1.0
QLOS	0.0	1.0	0.0	1.0
NLOS	0.0	0.0	1.0	1.0
Recall	1.0	1.0	1.0	1.0
MCC		1.0		

(c) Confusion matrix for NB classifier

Accuracy	LOS	QLOS	NLOS	*Precision*
LOS	1.0	0.0	0.0	1.0
QLOS	0.286	0.714	0.0	0.714
NLOS	0.259	0.185	0.556	0.556
Recall	0.438	0.5	1.0	0.659
MCC		0.6635		

(d) Confusion matrix for EL classifier

Accuracy	LOS	QLOS	NLOS	*Precision*
LOS	0.938	0.063	0.0	0.938
QLOS	0.111	0.889	0.0	0.889
NLOS	0.038	0.024	0.938	0.938
Recall	0.938	0.8	1.0	0.927
MCC		0.8829		

TABLE 8. Computational time for training and validation.

Classifier type	Computation time (s)
Multi-SVM	0.28
DT	0.09
NB	3.76
EL	2.60

acceptable performance, it is slightly more computationally expensive, and the NB classifier always performs worst, both in terms of accuracy and computational speed.

F. FEATURE RANKING AND SELECTION

1) FULL FEATURE SET

Despite satisfactory classification accuracy being achieved by the supervised learning classifier, it is also useful to check the ranking of the adopted small-scale fading features, i.e., which of these features contributes most during the classification stage. As described in Section. II-C, the dimension of the adopted features is $N \times 67$ and for the purpose of brevity, this feature set is denoted as *Full* feature set herein.

In order to produce the ranking of the *Full* feature set, we utilize the *ReliefF* algorithm described in [33]. The *ReliefF* algorithm is based on KNN and the main concept behind *ReliefF* is that for the feature f, *ReliefF* searches for k (here k stands for the k nearest neighbors in KNN) near hits from one particular class, i.e., the closest inter-class instances, and k near misses from each different class, i.e., the closest intra-class instances. Afterwards, the differences between the intra-class's and inter-class's distance are compared, then the weight of feature f will be increased if the inter-class's distance is larger than the intra-class's and vice versa. Finally, the rank of various features will be produced based on the corresponding weights, with positive and larger values of weight receiving the highest rankings. *ReliefF* is a good choice in domains with strong inter-dependencies between features for multi-class classification problem [33]. Since the value of k is user-defined and affects the ranking results, various k values were carefully investigated and then chosen so that the feature ranking results reached were stable and thus reliable.

The first ten feature ranking results of the *Full* feature set for the UE use case and user orientation classification are provided in Tables 9 and 10. In Table 9, for the *mobile* scenarios, the Nakagami m parameter and Rice $\mathcal{K}$ factor rank first and fourth, respectively, indicating that m and $\mathcal{K}$ values vary for different UE use cases and thus could be used to classify UE use cases for mobile users at mmWave frequencies. It is interesting to note that the LCR values between -2 dB and $+2$ dB are all within top nine ranks, indicating that the main differences between the small-scale fading observed for the mobile *Call*, *App* and *Pocket* cases occur close to the zero threshold level (i.e., mean). Nonetheless, for the *static* scenarios, both the Nakagami m parameter and Rice $\mathcal{K}$ factor

E. COMPUTATIONAL COST

Another significant issue for human activity recognition in mmWave networks is the computational cost for training and validating the machine learning model. Table 8 shows the time taken to train and validate models for the various classifiers. The workstation used in this study featured an Intel(R) Core(TM) i7-6700 CPU operating at 3.40 GHz with 16.0 GB of RAM. Table 8 shows that the DT and multi-SVM classifiers outperformed the other classifiers when considering computational time (0.09s and 0.28s, respectively), while the EL and NB classifiers were most computationally costly (with times of 2.60s and 3.76s respectively). Taking the accuracy and computational performance into account, the DT classifier is undoubtedly the best choice for mmWave UE use case recognition, while the multi-SVM classifier has

TABLE 9. Ranking of *Full* feature set for UE use case classification in the *mobile* and *static* scenarios.

Rank	Features (*mobile* scenarios)	Features (*static* scenarios)
1	Nakagami m	$\mathcal{T}_c(\gamma = 0)$
2	$\mathcal{T}_c(\gamma = 0)$	$\mathcal{T}_c(\gamma = 0.5)$
3	LCR($\delta = 0$)	Var
4	Rice $\mathcal{K}$	LCR($\delta = -8$)
5	LCR($\delta = +1$)	AFD($\delta = +4$)
6	LCR($\delta = -1$)	AFD($\delta = -9$)
7	$\mathcal{T}_c(\gamma = 0.5)$	LCR($\delta = -7$)
8	LCR($\delta = +2$)	AFD($\delta = -6$)
9	LCR($\delta = -2$)	AFD($\delta = +3$)
10	AFD($\delta = -16$)	LCR($\delta = -5$)

TABLE 10. Ranking of *Full* feature set for user orientation classification in the *static* scenarios.

Rank	Features (*Call* case)	Features (*App* case)	Features (*Pocket* case)
1	Var	$\mathcal{T}_c(\gamma = 0)$	$\mathcal{T}_c(\gamma = 0)$
2	LCR($\delta = -1$)	Var	LCR($\delta = +4$)
3	LCR($\delta = -4$)	AFD($\delta = +3$)	LCR($\delta = +3$)
4	$\mathcal{T}_c(\gamma = 0)$	LCR($\delta = 0$)	LCR($\delta = -9$)
5	LCR($\delta = -2$)	LCR($\delta = +2$)	Var
6	LCR($\delta = +2$)	AFD($\delta = +2$)	LCR($\delta = +2$)
7	LCR($\delta = 0$)	LCR($\delta = +1$)	LCR($\delta = -12$)
8	LCR($\delta = +3$)	LCR($\delta = -1$)	LCR($\delta = -8$)
9	AFD($\delta = +3$)	AFD($\delta = 0$)	LCR($\delta = -13$)
10	LCR($\delta = -6$)	AFD($\delta = +4$)	LCR($\delta = -1$)

are not in the top ten rank, while the $\mathcal{T}_c(\gamma = 0)$, $\mathcal{T}_c(\gamma = 0.5)$ and Var take the top three places. In Table 10, it can be seen that the Var is ranked within top five features to classify the user orientation for all three UE use cases in the *static* scenarios. Moreover, different ranges of the threshold δ for LCR and AFD are observed for the various UE use cases, e.g. under the *App* case, δ is between -1 dB to $+4$ dB for the first ten ranked features, while δ is between -13 dB and $+4$ dB for the *Pocket* case. The reason for this is that the UE was positioned at a lower elevation for the *Pocket* case, thus the shadowing resulted in a more significant difference between the LOS, QLOS and NLOS scenarios than that under the *App* case.

2) REDUCED FEATURE SET
As seen in Tables 9 and 10, it can be concluded that the Nakagami m parameter and Rice $\mathcal{K}$ factor are crucial features when classifying UE use cases for the *mobile* scenarios. Also that Var, $\mathcal{T}_c(\gamma = 0.5)$, $\mathcal{T}_c(\gamma = 0)$, as well as LCR and AFD with δ between -2 and $+2$ dB play important roles when classifying UE use cases and user orientations for the *static* scenarios. Therefore, aiming to reduce the complexity and computation resources required for the classification system,

Var, the Rice $\mathcal{K}$ factor, the Nakagami m parameter, $\mathcal{T}_c(\gamma = 0.5)$, $\mathcal{T}_c(\gamma = 0)$, and LCR and AFD with δ between -2 and $+2$ dB are selected from the *Full* feature set to form a new feature set, denoted the *Reduced* feature set. Consequently, the dimension of the adopted features is reduced to $N \times 15$. As shown in Section V-C to V-E, the DT classifier provided the best accuracy and computation performance, thus it is chosen to investigate the performance of the *Reduced* feature set.

The confusion matrix of the *Reduced* feature set for the DT classifier is provided in Table 11. Compared to the *Full* feature set performance for the DT classifier in Tables 2, 5, 6 and 7, as expected, the classification accuracy of the *Reduced* feature is decreased, e.g. for *mobile* scenarios, the UE use classification accuracy dropped slightly from 100% (MCC: 1.0) for the *Full* feature set to 94.7% (MCC: 0.9245). Significantly, it can be observed the feature reduction has a larger impact on the user orientation classification performance of the *App* and *Pocket* cases compared to the other cases, e.g. the classification accuracy declined significantly from 92.7% (MCC: 0.8894) to 83.8% (MCC: 0.7361) for the *App* case.

3) CONSTRAINED FEATURE SET
Though the *Full* and *Reduced* feature sets have provided favorable classification accuracy, it is noted that the Rice $\mathcal{K}$ factor and Nakagami m parameter need to be estimated using MLE. The process of obtaining maximum likelihood estimates is usually computationally expensive, thus it may not be favorable for UE usage identification in real time communications. Therefore, Var, $\mathcal{T}_c(\gamma = 0)$, and LCR($\delta = 0$) were further selected to form a *Constrained* feature set. As a result, the dimension of the *Constrained* feature set is limited to $N \times 3$.

The confusion matrix of the *Constrained* feature set for DT classifier is shown in Table 12. Intuitively, it is interesting to observe that compared to the *Reduced* feature set performance in Table 11, the feature reduction in the *Constrained* feature set has a greater impact on the UE use case classification performance in the *mobile* case than the *static* case. For example, the UE use case classification accuracy for the *mobile* case deteriorates from 94.7% (MCC: 0.9245) to 86.8% (MCC: 0.8546) while the classification accuracy decreases from 89.8% (MCC: 0.8509) to 87.8% (MCC: 0.8282) in the *static* case. This further verifies the significance of the Rice $\mathcal{K}$ factor, the Nakagami m parameter as well as the LCR and AFD values around the zero threshold level during the UE use case classification process in the *mobile* case, which corresponds to the ranking result in Table 9. Moreover, it can be seen that for the *Constrained* feature set, the classification performance deteriorates under the *App* and *Pocket* use cases, e.g. compared to the *Reduced* feature set performance in Table 11, the classification accuracy under the *Pocket* use case declined substantially from 82.9% (MCC: 0.743) to 70.7% (MCC: 0.5689). This is in contrast to the *Call* scenario where the classification accuracy is maintained at 92.9%

TABLE 11. Confusion matrix of *Reduced* feature set for DT classifier.

(a) Confusion matrix for the *mobile* scenario

Accuracy	Call	App	Pocket	*Precision*
Call	0.938	0.062	0.0	0.938
App	0.0	0.909	0.091	0.909
Pocket	0.0	0.0	1.0	1.0
Recall	1.0	0.909	0.917	0.947
MCC		0.9245		

(b) Confusion matrix for the *static* scenario

Accuracy	Call	App	Pocket	*Precision*
Call	1.0	0.0	0.0	1.0
App	0.105	0.842	0.053	0.842
Pocket	0.0	0.143	0.857	0.857
Recall	0.889	0.889	0.923	0.898
MCC		0.8509		

(c) Confusion matrix for the *Call* case (*static*)

Accuracy	LOS	QLOS	NLOS	*Precision*
LOS	0.944	0.056	0.0	0.944
QLOS	0.053	0.894	0.053	0.894
NLOS	0.0	0.053	0.947	0.947
Recall	0.944	0.894	0.947	0.929
MCC		0.8925		

(d) Confusion matrix for the *App* case (*static*)

Accuracy	LOS	QLOS	NLOS	*Precision*
LOS	0.933	0.067	0.0	0.933
QLOS	0.4	0.6	0.0	0.6
NLOS	0.0	0.083	0.917	0.917
Recall	0.778	0.75	1.0	0.838
MCC		0.7361		

(e) Confusion matrix for the *Pocket* case (*static*)

Accuracy	LOS	QLOS	NLOS	*Precision*
LOS	0.857	0.143	0.0	0.857
QLOS	0.154	0.615	0.231	0.615
NLOS	0.0	0.0	1.0	1.0
Recall	0.857	0.8	0.824	0.829
MCC		0.743		

TABLE 12. Confusion matrix for *Constrained* feature set for DT classifier.

(a) Confusion matrix for the *mobile* scenario

Accuracy	Call	App	Pocket	*Precision*
Call	1.0	0.0	0.0	1.0
App	0.125	0.688	0.187	0.688
Pocket	0.0	0.0	1.0	1.0
Recall	0.833	1.0	0.8	0.868
MCC		0.8546		

(b) Confusion matrix for the *static* scenario

Accuracy	Call	App	Pocket	*Precision*
Call	0.889	0.111	0.0	0.889
App	0.083	0.917	0.0	0.917
Pocket	0.0	0.158	0.842	0.842
Recall	0.941	0.688	1.0	0.878
MCC		0.8282		

(c) Confusion matrix for the *Call* case (*static*)

Accuracy	LOS	QLOS	NLOS	*Precision*
LOS	1.0	0.0	0.0	1.0
QLOS	0.053	0.894	0.053	0.894
NLOS	0.0	0.1	0.9	0.9
Recall	0.944	0.894	0.947	0.929
MCC		0.8974		

(d) Confusion matrix for the *App* case (*static*)

Accuracy	LOS	QLOS	NLOS	*Precision*
LOS	0.833	0.167	0.0	0.833
QLOS	0.154	0.462	0.384	0.462
NLOS	0.0	0.0	1.0	1.0
Recall	0.833	0.75	0.706	0.757
MCC		0.6635		

(e) Confusion matrix for the *Pocket* case (*static*)

Accuracy	LOS	QLOS	NLOS	*Precision*
LOS	0.75	0.25	0.0	0.75
QLOS	0.231	0.462	0.307	0.462
NLOS	0.0	0.083	0.917	0.917
Recall	0.8	0.545	0.733	0.707
MCC		0.5689		

(MCC here is between 0.8925 and 0.8974). Since the Rice $\mathcal{K}$ factor and Nakagami m parameter are not within the top ten ranks in Table 10, it can be inferred that in addition to the zero threshold level, the LCR and AFD must be considered over wider ranges in order to achieve a higher UE orientation classification accuracy for the *App* and *Pocket* use cases.

G. PERFORMANCE COMPARISON WITH PREVIOUS WORK

A performance comparison between this work and previous RSS/RSSI-based user activities/usage recognition work is provided in Table 13. Due to the much shorter wavelengths which exist in mmWave bands and the more profound effect that the human body has on signal propagation at these frequencies, a higher resolution of user activities/usage can be

TABLE 13. Performance comparisons of RSS/RSSI-based user activities/usages recognition works.

Work	Frequency band	Activities/Usages	Accuracy
Xiao *et al.* [14]	Wi-Fi band (sub 6 GHz)	LOS and NLOS (*static* and *dynamic*)	up to 95%
Geng *et al.* [18]	2.45 GHz	*Standing*, *walking*, *running*, *crawling*, etc	82.7% − 90.4%
Archasantisuk *et al.* [20]	403.5 MHz and 2.45 GHz	*Running*, *walking*, *sitting*, *sleeping*, etc.	63.8% − 95.7%
Chi *et al.* [21]	2.4 GHz	*Walking*, *sitting*, *falling*, *running*, etc.	74% − 90%
Palumbo *et al.* [26]	2.4 GHz	*Bending*, *cycling*, *laying*, *sitting*, etc.	95.6% − 98.8%
Kawakami *et al.* [27]	LTE band	*Static*, *walking*, *bicycle*, *bus*, *train*, etc	77.0% − 96.5%
Zhang *et al.* [this work]	60 GHz	*Call*, *App*, and *Pocket* (*mobile* and *static*)	98.2% − 100%
		LOS, QLOS and NLOS (*mobile* and *static*)	97.6% − 100%

achieved. This can be seen from Table 13, as compared to previous work which considered traditional Wi-Fi or LTE bands along with multiple APs, in this study only a single centralized mmWave AP was used, yet a much higher classification accuracy was obtained, e.g., the classification of UE use usages can be achieved with an accuracy between 98.2% and 100%, while the user orientations can also be estimated with high accuracy (between 97.6% and 100%).

VI. CONCLUSION AND FUTURE WORK
In this work, we have presented a novel supervised and unsupervised learning approach to automatically recognize user states and UE use cases based on the extraction of RSS statistical features for mmWave indoor scenarios. Extensive measurements were performed using a custom 60 GHz wireless measurement system for realistic indoor scenarios involving a UE and a ceiling mounted wireless AP. It was established that, for the considered activities, a sliding window length of 1s without overlap was the best choice for time series segmentation at 60 GHz. A range of supervised machine learning algorithms were applied and the results showed that the DT classifier outperformed all other classifiers with an accuracy of 100% and 98.0% for *mobile* and *static* scenarios, respectively. For a static user, their orientation could also be correctly estimated using the DT classifier with an accuracy of 98.2%, 97.6% and 100% for the *Call*, *App* and *Pocket* use cases, respectively. Also, the computational time required for the DT classifier to reach a decision was much lower than the others considered. Furthermore, the small-scale fading features used in this study were ranked during the training stage and it was found that, when it is desired to classify UE use cases under *mobile* conditions, the Nakagami *m* parameter, Rice $\mathcal{K}$ factor, and LCR around the zero threshold level contributed the most useful information. In the *static* scenarios, variance, channel coherence time and LCR/AFD were found to provide the greatest influence. Additionally, it was demonstrated that the orientation of a static user can be recognized by exploring the differences of the variance, channel coherence time and LCR/AFD. Finally, considering the requirements of a real time wireless communication system, we compared the system classification performance

for the *Full*, *Reduced*, and *Constrained* feature sets. It was determined that feature reduction had a pronounced impact on the user orientation classification performance for the *App* and *Pocket* use cases, with the accuracy decreasing from 92.7% to 75.7% and 85.4% to 70.7% for the *App* and *Pocket* use cases, respectively. In contrast, the feature reduction was observed to have a lesser effect when classifying the UE use cases in both *mobile* and *static* scenarios.

Although the results obtained here show much promise for using the RSS as a UE usage mode classifier, many open research challenges remain which should be explored in the future work. One drawback of supervised learning is, the model has to learn from the labeled training data and, compared to an unsupervised learning approach, the labeling process usually requires extra labor or computational costs. Therefore, it is recommended that completely unsupervised learning approaches, such as self-organizing map (SOM), should be investigated. As observed in this study, the interchange between user states and UE usage scenarios can lead to inaccurate labeling of the data. Therefore using a variable window size or type based on different user activities as introduced in [36], could be advantageous for practical deployment of the techniques proposed in this paper. It is worth highlighting that the use of a variable window size or type could also be extended to inform feature selection, e.g., as highlighted in [36], a larger size of window is often required when a smaller number of feature sets are selected, and vice versa. In addition, since the primary objective of the work undertaken in this study was to understand the potential of using the RSS to classify UE usage in the presence of the operator, future work should also take into account other factors which can affect the RSS such as pedestrian activity in the vicinity of the target UE.

REFERENCES
[1] S. A. Busari, S. Mumtaz, S. Al-Rubaye, and J. Rodriguez, "5G millimeter-wave mobile broadband: Performance and challenges," *IEEE Commun. Mag.*, vol. 56, no. 6, pp. 137–143, Jun. 2018.

[2] Y. Ghasempour, C. R. C. M. Da Silva, C. Cordeiro, and E. W. Knightly, "IEEE 802.11ay: Next-generation 60 GHz communication for 100 Gb/s Wi-Fi," *IEEE Commun. Mag.*, vol. 55, no. 12, pp. 186–192, Dec. 2017.
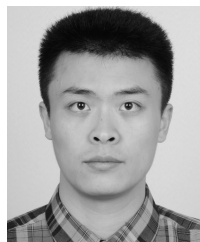
[3] P. Smulders, "Exploiting the 60 GHz band for local wireless multimedia access: Prospects and future directions," *IEEE Commun. Mag.*, vol. 40, no. 1, pp. 140–147, Jan. 2002.

[4] Y. Niu, Y. Li, D. Jin, L. Su, and A. V. Vasilakos, "A survey of millimeter wave communications (mmWave) for 5G: Opportunities and challenges," *Wireless Netw.*, vol. 21, no. 8, pp. 2657–2676, Nov. 2015.

[5] P. Smulders and G. Vervuurt, "Influence of antenna radiation patterns on MM-wave indoor radio channels," in *Proc. 2nd IEEE Int. Conf. Universal Pers. Commun.*, Dec. 2002, vol. 2, pp. 631–635.

[6] P. Smulders and A. Wagemans, "Biconical horn antennas for near uniform coverage in indoor areas at mm-wave frequencies," *IEEE Trans. Veh. Technol.*, vol. 43, no. 4, pp. 897–901, Nov. 1994.

[7] T. Manabe, Y. Miura, and T. Ihara, "Effects of antenna directivity and polarization on indoor multipath propagation characteristics at 60 GHz," *IEEE J. Sel. Areas Commun.*, vol. 14, no. 3, pp. 441–448, Apr. 1996.

[8] P. Marinier, G. Delisle, and C. Despins, "Influence of human motion on indoor wireless millimeter-wave channel characteristics," in *Proc. IEEE 47th Veh. Technol. Conf. Technol. Motion*, vol. 2, May 1997, pp. 979–983.

[9] S. K. Yoo, S. L. Cotton, R. W. Heath, and Y. J. Chun, "Measurements of the 60 GHz UE to eNB channel for small cell deployments," *IEEE Wireless Commun. Lett.*, vol. 6, no. 2, pp. 178–181, Apr. 2017.

[10] S. K. Yoo, S. L. Cotton, Y. J. Chun, W. G. Scanlon, and G. A. Conway, "Channel characteristics of dynamic off-body communications at 60 GHz under line-of-sight (LOS) and non-LOS conditions," *IEEE Antennas Wireless Propag. Lett.*, vol. 16, pp. 1553–1556, 2017.

[11] O. D. Lara and M. A. Labrador, "A survey on human activity recognition using wearable sensors," *IEEE Commun. Surveys Tuts.*, vol. 15, no. 3, pp. 1192–1209, 3rd Quart., 2013.

[12] M. A. Alsheikh, D. Niyato, S. Lin, H.-P. Tan, and Z. Han, "Mobile big data analytics using deep learning and Apache spark," *IEEE Netw.*, vol. 30, no. 3, pp. 22–29, May 2016.

[13] O. Yurur, C. H. Liu, Z. Sheng, V. C. M. Leung, W. Moreno, and K. K. Leung, "Context-awareness for mobile sensing: A survey and future directions," *IEEE Commun. Surveys Tuts.*, vol. 18, no. 1, pp. 68–93, 1st Quart., 2016.

[14] Z. Xiao, H. Wen, A. Markham, N. Trigoni, P. Blunsom, and J. Frolik, "Non-line-of-sight identification and mitigation using received signal strength," *IEEE Trans. Wireless Commun.*, vol. 14, no. 3, pp. 1689–1702, Mar. 2015.

[15] J. Wang, L. Zhang, Q. Gao, M. Pan, and H. Wang, "Device-free wireless sensing in complex scenarios using spatial structural information," *IEEE Trans. Wireless Commun.*, vol. 17, no. 4, pp. 2432–2442, Apr. 2018.

[16] H. Jiang, C. Cai, X. Ma, Y. Yang, and J. Liu, "Smart home based on WiFi sensing: A survey," *IEEE Access*, vol. 6, pp. 13317–13325, 2018.

[17] J. Liu, H. Liu, Y. Chen, Y. Wang, and C. Wang, "Wireless sensing for human activity: A survey," *IEEE Commun. Surveys Tuts.*, early access, 2019, doi: 10.1109/COMST.2019.2934489.

[18] Y. Geng, J. Chen, R. Fu, G. Bao, and K. Pahlavan, "Enlighten wearable physiological monitoring systems: On-body RF characteristics based human motion classification using a support vector machine," *IEEE Trans. Mobile Comput.*, vol. 15, no. 3, pp. 656–671, Mar. 2016.

[19] C.-W. Hsu and C.-J. Lin, "A comparison of methods for multiclass support vector machines," *IEEE Trans. Neural Netw.*, vol. 13, no. 2, pp. 415–425, Mar. 2002.

[20] S. Archasantisuk, T. Aoyagi, T. Uusitupa, M. Kim, and J.-I. Takada, "Human motion classification using radio signal strength in WBAN," *IEICE Trans. Commun.*, vol. 99, no. 3, pp. 592–601, 2016.

[21] Z. Chi, Y. Yao, T. Xie, Z. Huang, M. Hammond, and T. Zhu, "Harmony: Exploiting coarse-grained received signal strength from IoT devices for human activity recognition," in *Proc. IEEE 24th Int. Conf. Netw. Protocols (ICNP)*, Nov. 2016, pp. 1–10.

[22] A. Wang, G. Chen, J. Yang, S. Zhao, and C.-Y. Chang, "A comparative study on human activity recognition using inertial sensors in a smartphone," *IEEE Sensors J.*, vol. 16, no. 11, pp. 4566–4578, Jun. 2016.

[23] A. McCallum and K. Nigam, "A comparison of event models for naive Bayes text classification," in *Proc. AAAI Workshop Learn. Text Categorization*, 1998, vol. 752, no. 1, pp. 41–48.

[24] T. Cover and P. Hart, "Nearest neighbor pattern classification," *IEEE Trans. Inf. Theory*, vol. TIT-13, no. 1, pp. 21–27, Jan. 1967.

[25] Z. Chen, L. Zhang, Z. Cao, and J. Guo, "Distilling the knowledge from handcrafted features for human activity recognition," *IEEE Trans. Ind. Informat.*, vol. 14, no. 10, pp. 4334–4342, Oct. 2018.

[26] F. Palumbo, C. Gallicchio, R. Pucci, and A. Micheli, "Human activity recognition using multisensor data fusion based on Reservoir Computing," *J. Ambient Intell. Smart Environ.*, vol. 8, no. 2, pp. 87–107, Mar. 2016.

[27] W. Kawakami, K. Kanai, B. Wei, and J. Katto, "A highly accurate transportation mode recognition using mobile communication quality," *IEICE Trans. Commun.*, vol. 102, no. 4, pp. 741–750, Apr. 2019.

[28] Y. Oguma, T. Nishio, K. Yamamoto, and M. Morikura, "Proactive handover based on human blockage prediction using RGB-D cameras for mmWave communications," *IEICE Trans. Commun.*, vol. 99, no. 8, pp. 1734–1744, 2016.

[29] Microsoft. *Kinect for Windows*. Accessed: Jan. 9, 2020. [Online]. Available: https://developer.microsoft.com/en-us/windows/kinect

[30] H. Okamoto, T. Nishio, M. Morikura, K. Yamamoto, D. Murayama, and K. Nakahira, "Machine-learning-based throughput estimation using images for mmWave communications," in *Proc. IEEE 85th Veh. Technol. Conf. (VTC Spring)*, Jun. 2017, pp. 1–6.

[31] J. R. Quinlan, "Induction of decision trees," *Mach. Learn.*, vol. 1, no. 1, pp. 81–106, 1986.

[32] L. I. Kuncheva, *Combining Pattern Classifiers: Methods and Algorithms*. Hoboken, NJ, USA: Wiley, 2004.

[33] H. Liu and H. Motoda, *Computational Methods of Feature Selection*. Boca Raton, FL, USA: CRC Press, 2007.

[34] K. Turbic, S. J. Ambroziak, and L. M. Correia, "Characteristics of the polarised off-body channel in indoor environments," *EURASIP J. Wireless Commun. Netw.*, vol. 2017, no. 1, p. 174, Oct. 2017.

[35] T. Otim, A. Bahillo, L. E. Diez, P. Lopez-Iturri, and F. Falcone, "FDTD and empirical exploration of human body and UWB radiation interaction on TOF ranging," *IEEE Antennas Wireless Propag. Lett.*, vol. 18, no. 6, pp. 1119–1123, Jun. 2019.

[36] O. Banos, J.-M. Galvez, M. Damas, H. Pomares, and I. Rojas, "Window size impact in human activity recognition," *Sensors*, vol. 14, no. 4, pp. 6474–6499, Apr. 2014.

[37] S. K. Yoo, S. L. Cotton, W. G. Scanlon, and G. A. Conway, "An experimental evaluation of switched combining based macro-diversity for wearable communications operating in an outdoor environment," *IEEE Trans. Wireless Commun.*, vol. 16, no. 8, pp. 5338–5352, Aug. 2017.

[38] S. Lloyd, "Least squares quantization in PCM," *IEEE Trans. Inf. Theory*, vol. TIT-28, no. 2, pp. 129–137, Mar. 1982.

[39] S. O. Rice, "Mathematical analysis of random noise," *Bell System Tech. J.*, vol. 24, no. 1, pp. 282–332, Jan. 1945.

[40] M. Nakagami, "The m-distribution—A general formula of intensity distribution of rapid fading," in *Statistical Methods in Radio Wave Propagation*. Amsterdam, The Netherlands: Elsevier, 1960, pp. 3–36.

[41] G. E. Box, G. M. Jenkins, G. C. Reinsel, and G. M. Ljung, *Time Series Analysis, Forecasting and Control*. Hoboken, NJ, USA: Wiley, 2015.

[42] J. D. Parsons, *The Mobile Radio Propagation Channel*. Hoboken, NJ, USA: Wiley, 2000.

[43] S. Ki Yoo, S. Cotton, Y. Jin Chun, and W. Scanlon, "Fading characterization of UE to ceiling-mounted access point communications at 60 GHz," in *Proc. 12th Eur. Conf. Antennas Propag. (EuCAP)*, 2018, pp. 1–5.

[44] T. S. Rappaport, *Wireless Communications: Principles and Practice*, vol. 2. Upper Saddle River, NJ, USA: Prentice-Hall, 1996.

[45] I. Guyon and A. Elisseeff, "An introduction to variable and feature selection," *J. Mach. Learn. Res.*, vol. 3, pp. 1157–1182, Jan. 2003.

[46] S. Aksoy and R. M. Haralick, "Feature normalization and likelihood-based similarity measures for image retrieval," *Pattern Recognit. Lett.*, vol. 22, no. 5, pp. 563–582, Apr. 2001.

[47] T. Poggio and S. Edelman "A network that learns to recognize three-dimensional objects," *Nature*, vol. 343, no. 6255, p. 263, 1990.

[48] A. Coates and A. Y. Ng, "Learning feature representations with K-means," in *Neural Networks: Tricks of the Trade*. Springer, 2012, pp. 561–580.

[49] S. Ioffe and C. Szegedy, "Batch normalization: Accelerating deep network training by reducing internal covariate shift," in *Proc. Int. Conf. Mach. Learn.*, vol. 37. Jul. 2015, pp. 448–456.

[50] T. Joachims, "Text categorization with support vector machines: Learning with many relevant features," in *Proc. Eur. Conf. Mach. Learn.*, 1998, pp. 137–142.

[51] R. Kohavi, "A study of cross-validation and bootstrap for accuracy estimation and model selection," in *Proc. Int. Joint Conf. AI*, Aug. 1995, vol. 14. no. 2, pp. 1137–1145.

[52] L. Zhang, A. Mckernan, S. Cotton, and W. Scanlon, "The influence of elevation angle on 60 GHz near-body path gain," in *Proc. 12th Eur. Conf. Antennas Propag. (EuCAP)*, 2018, pp. 1–5.

[53] S. K. Yoo, N. Bhargav, S. L. Cotton, P. C. Sofotasios, M. Matthaiou, M. Valkama, and G. K. Karagiannidis, "The κ-μ/inverse gamma and η-μ/inverse gamma composite fading models: Fundamental statistics and empirical validation," *IEEE Trans. Commun.*, early access, 2017, doi: 10.1109/TCOMM.2017.2780110.

[54] D. M. Powers, "Evaluation: From precision, recall and F-measure to ROC, informedness, markedness and correlation," *J. Mach. Learn. Technol.*, vol. 2, no. 1, pp. 37–63, 2011.

[55] B. Matthews, "Comparison of the predicted and observed secondary structure of T4 phage lysozyme," *Biochimica et Biophys. Acta (BBA)-Protein Struct.*, vol. 405, no. 2, pp. 442–451, Oct. 1975.

[56] J. Gorodkin, "Comparing two K-category assignments by a K-category correlation coefficient," *Comput. Biol. Chem.*, vol. 28, nos. 5–6, pp. 367–374, Dec. 2004.

[57] D. Cassioli and N. Rendevski, "A statistical model for the shadowing induced by human bodies in the proximity of a mmWaves radio link," in *Proc. IEEE Int. Conf. Commun. Workshops (ICC)*, Jun. 2014, pp. 14–19.

SEONG KI YOO (Member, IEEE) received the B.Eng. degree (Hons.) in telecommunication systems from the University of Surrey, Guildford, U.K., in 2010, the M.Sc. degree in communications and signal processing from Imperial College London, London, U.K., in 2012, and the Ph.D. degree from Queen's University Belfast, Belfast, U.K., in 2017. His Ph.D. studies were sponsored by U.K. EPSRC. He was a Junior Researcher with the Korea Electrotechnology Research Institute (KERI), Ansan, South Korea, from 2012 to 2013. He is currently a Lecturer with the School of Computing, Electronics and Mathematics, Coventry University. His research interests include mmWave channel modeling and measurements, fading characterization for wearable and vehicular communications channels, and performance analysis over fading channels.

LEI ZHANG (Student Member, IEEE) received the B.Sc. degree in communication engineering from Shandong University, China, in 2012, and the M.Sc. degree in communication and information technology from the University of Bremen, Germany, in 2016. He is currently pursuing the Ph.D. degree with the Centre for Wireless Innovation (CWI), ECIT Institute, Queen's University Belfast, Belfast, U.K. His research interests include millimeter-wave channel modeling and measurements, machine learning for wireless communications, fading characterization for body-centric communications, and 5G wireless communications.

YANG HUA received the Ph.D. degree from Université Grenoble Alpes/Inria Grenoble Rhône-Alpes, France, funded by Microsoft Research—Inria Joint Center. He worked as a Senior Research and Development Engineer at Panasonic Singapore Laboratories, Singapore, for four years. He is currently a Lecturer with EEECS/ECIT, Queens University of Belfast, U.K. He holds three U.S. patents and one China patent and received four titles of prestigious international competitions, including PASCAL Visual Object Classes (VOC) Challenge Classification Competition and the Thermal Imagery Visual Object Tracking (VOT-TIR) Competition.

CLAUDIO R. C. M. DA SILVA (Senior Member, IEEE) received the Ph.D. degree in electrical engineering from the University of California at San Diego, San Diego, in 2005. He first worked as an Assistant Professor at Virginia Tech and later became a member of the Samsung Mobile Solutions Lab, when he was engaged in cellular modem implementation and applied research. He is currently a Systems Engineer with the Wireless Connectivity Standards Group, Intel Corporation, and has several years of experience in wireless communication system design, prototyping, and development. He has been an active contributor to various IEEE 802.11 activities, including the development of IEEE 802.11ay (Next Generation 60 GHz) and the creation of a WLAN sensing effort. He has served on the technical program committee of numerous IEEE conferences in the communications area. He was an Editor of the IEEE TRANSACTIONS ON COMMUNICATIONS.

SIMON L. COTTON (Senior Member, IEEE) received the B.Eng. degree in electronics and software from Ulster University, Ulster, U.K., in 2004, and the Ph.D. degree in electrical and electronic engineering from the Queen's University of Belfast, Belfast, U.K., in 2007. From 2007 to 2011, he was a Research Fellow and a Senior Research Fellow, from 2011 to 2012, a Lecturer (Assistant Professor), from 2012 to 2015, and a Reader (Associate Professor), from 2015 to 2019 with the Queen's University of Belfast. He is currently a Full Professor and the Director of the Centre for Wireless Innovation (CWI), Queen's University Belfast. He has authored and coauthored more than 140 publications in major IEEE/IET journals and refereed international conferences, two book chapters, and two patents. Among his research interests are cellular device-to-device, vehicular, and body-centric communications. His other research interests include radio channel characterization and modeling, and the simulation of wireless channels. He received the H. A. Wheeler Prize, in July 2010, by the IEEE Antennas and Propagation Society for the best applications journal article in the IEEE TRANSACTIONS ON ANTENNAS AND PROPAGATION, in 2009. In July 2011, he received the Sir George Macfarlane Award from the U.K. Royal Academy of Engineering in recognition of his technical and scientific attainment since graduating from his first degree in engineering.

WILLIAM G. SCANLON (Fellow, IEEE) was a Senior Lecturer and a Chair/Full Professor with the Queen's University of Belfast, U.K., from 2002 to 2018. He held various leadership positions such as the Director of the Centre for Wireless Innovation and the Head of the School of Electronics, Electrical Engineering and Computer Science. He held a part-time Chair in short range radio with the University of Twente, The Netherlands, from 2009 to 2014. He is currently a Chief Executive Officer of the Tyndall National Institute, Ireland. He is a pioneer in wearable and implantable medical device communications. He has served as a Keynote Speaker for the International Symposium on Antennas and Propagation in 2018, the IEEE International Microwave Workshop Series on RF and Wireless Technologies for Biomedical and Healthcare Applications in 2014, the NATO Military Communications and Information Systems Conference in 2010, the International Conference on Bodynets in 2010 and 2018, and the European Workshop on Conformal Antennas in 2007. He was a Series Editor of the IET Book Series on Telecommunications and Networking, an Inaugural Associate Editor of IEEE JOURNAL OF TRANSLATIONAL ENGINEERING IN HEALTH AND MEDICINE and an Associate Editor of the IEEE ANTENNAS AND WIRELESS PROPAGATION LETTERS. He holds an URSI Young Scientist Award in 1999, the 2010 IEEE H. A. Wheeler Prize Paper Award for the IEEE TRANSACTIONS ON ANTENNAS AND PROPAGATION, He delivered the 2012 NATO International Lecture Series on Next Generation Communications.

• • •